Title: Mechanical imbalance between normal and cancer cells drives epithelial defense against cancer

Praver Gupta[1], Sayantani Kayal[2], Shilpa P. Pothapragada[1,3], Harish K. Senapati[1,4], Padmashree Devendran[1], Dapeng Bi[2,*], and Tamal Das[1,*]

1. Tata Institute of Fundamental Research Hyderabad (TIFR-H), Hyderabad 500046, India
2. Department of Physics, Northeastern University, Boston, MA 02115, USA
3. Present address: Wyss Institute for Biologically Inspired Engineering, Harvard University, Boston, MA 02115. USA
4. Present address: Max Planck Institute for Medical Research, Heidelberg 69120, Germany

[*]All correspondence related to theory and experiments should be addressed to D.B. (Email: d.bi@northeastern.edu) and T.D. (Email: tdas@tifrh.res.in), respectively.

Keywords: Physics of cancer, Cell competition, Tissue stress, Compressibility, Mechanical imbalance

ABSTRACT

Cell competition enables normal wildtype cells of epithelial tissue to eliminate mutant cells expressing activated oncoproteins such as $HRas^{V12}$. However, the driving force behind this fundamental epithelial defense against cancer remains enigmatic. Here, we employ tissue stress microscopy and theoretical modeling and invent a new collective compressibility measurement technique called gel compression microscopy to unveil the mechanism governing cell competition. Stress microscopy reveals unique compressive stress experienced by the mutant cells, contrasting with predominantly tensile stress experienced by normal cells. A cell-based computer simulation then predicts that this compressive stress arises out of a mechanical imbalance between two competing populations due to a difference in their collective compressibility and rigidity. Gel compression microscopy empirically confirms the prediction and elucidates a three-fold higher compressibility of the mutant population than the normal population. Mechanistically, this difference stems from the reduced abundance and coupling of junctional E-cadherin molecules in the mutant cells, which weakens cell-cell adhesions and renders the mutant population more compressible. Taken together, our study elucidates both the physical principle and the underlying molecular mechanism driving cell competition in epithelial defense against cancer and opens new directions for mechanomedicine in cancer.

Epithelial defense against cancer (EDAC) is a non-cell autonomous removal of transformed mutant cells expressing constitutively active forms of oncoproteins such as HRas^{V12} [1-4]. It belongs to a broad class of non-cell autonomous cell-elimination processes called cell competition, which, besides EDAC, controls organ development, tissue quality control, and ageing[5,6]. During EDAC, normal epithelial cells eliminate the mutant cells from the tissue by apical extrusion or by basal delamination[3]. Despite some recent progress, the mechanisms underlying how normal cells recognize and eliminate the mutant cells remain largely elusive[1]. The competitive removal of mutant cells requires extensive reorganization of force-bearing cytoskeletal elements in the surrounding normal cells, particularly at the interface between normal and mutant cells[7-9]. The process additionally depends on the mechanics of the extracellular matrix[10], indicating possible modulations of cellular mechanical forces during EDAC[9,11-14].

Mechanical forces play critical roles during cell competition in general[9,11]. A differential in cell proliferation potential between two competing populations can drive out the population with a lower proliferation potential by compaction. Also, cells carrying distinct genetic lesions can have varying sensitivities to compaction, which might lead to their elimination[9]. This explains how a fast-growing population bearing higher resistance to deformation and elimination can have a competitive advantage over a slow-growing population[12,13,15,16]. However, it is not clear how cell elimination occurs when the proliferative differential is trivial. For example, the competitive elimination of epithelial cells expressing oncoprotein HRas^{V12} by normal wildtype epithelial cells is well-established in a model for EDAC[3,4,10], but proliferation differential might not be a critical factor here. In fact, we probed the growth potential of these populations by quantitating their number expansion in time, starting from a similar number density (Supplementary Figs. 1a-b). We also directly measured the proliferation rate using ethynyl deoxyuridine (EdU) labeling (Supplementary Figs. 1c-d). These experiments revealed that the difference in growth potential between mutant and wildtype populations is not significant. In fact, HRas^{V12}-expressing mutant cells show slightly higher proliferation post-48 hours of growth. Thus, in this model for EDAC, despite having a slightly higher growth rate, the mutant cells are eliminated during competition with normal cells. The mechanisms underlying this competitive elimination of the mutant cells by normal cells remain poorly understood. While it is possible that tissue and cell mechanics might play a crucial role here, in the absence of direct measurement of forces during EDAC, it is unclear how tissue mechanics regulates non-proliferative cell competition between the wildtype and mutant cells.

Competition-induced compression of the mutant population.

To elucidate the role of tissue mechanics in EDAC, we measured tissue forces in a model for cell competition, in which we utilized the competition between wildtype Madin-Darby canine kidney (MDCK) and HRas^{V12}-expressing mutant MDCK epithelial cells[3]. In this model, the expression of HRas^{V12} is dependent on the Tet-on system and is induced by a tetracycline derivative called doxycycline, enabling us to trigger cell-cell competition at will. We mixed wildtype and HRas^{V12}-expressing mutant cells in a 40:1 ratio (Supplementary Fig. 2a) so that in the absence of doxycycline, mutant cells would form small colonies (two-ten cells, Fig. 1a and Supplementary Fig. 2b), surrounded by wildtype cells. We then exposed this heterogeneous epithelial monolayer to a medium containing doxycycline, which induced HRas^{V12} expression in the mutant cells (Fig. 1a). This monolayer system thus mimicked an *in vivo* scenario where mutant cells appear in a normal tissue background[3,17]. We employed 4 kPa polyacrylamide gels as substrate for this model to mimic physiological stiffness[10]. Subsequently, mutant cells were extruded out of the monolayer (Supplementary Fig. 2b). However, we did not observe such extrusion in the homogenous HRas^{V12}-expressing monolayer. Only when these mutant cells interfaced wildtype cells in their vicinity, an active remodeling of the actomyosin occurred

towards the mutant-wildtype interface, as highlighted by distinct phosphorylated myosin II light chain (pMLC2, active form of myosin II motor[18]) surrounding mutant cells (Supplementary Fig. 2c). These results indicated that the extrusion of the HRas^{V12}-expressing cells from the heterogeneous monolayer is a non-cell autonomous process and requires physical contact between the two populations.

Next, to elucidate the change in the mechanical force field during cell competition, we combined traction force microscopy with Bayesian inverse stress microscopy[19] (Supplementary Fig. 2d). We also used Bayesian force inference[20] (Supplementary Fig. 2e) in another independent set of experiments. From traction force microscopy experiments, we observed that upon induction of HRas^{V12}-expression, traction forces increased along the interface between normal and transformed mutant populations (Fig. 1b and Supplementary Fig. 2h). Simultaneously, stress microscopy revealed local compressive stress appearing in the regions occupied by mutant cells (Fig. 1c and Supplementary Fig. 2h). We concluded that this compressive stress is a unique mechanical signature of cell competition since in a homogeneous population of either normal or mutant cells, stresses remained predominantly tensile (Supplementary Figs. 2f-g), as reported previously[19,21,22]. While the complete extrusion of mutant cells took at least six hours after the doxycycline exposure (Fig. 1a and Supplementary Fig. 2h), compressive stresses arose around two hours post-doxycycline exposure (Supplementary Fig. 2h), indicating that compressive stress precedes cell rounding up and extrusion (Supplementary video 1). In addition, compressive stress appeared to be restricted only to mutant cells as the background tissue comprising normal cells presented a predominantly tensile stress field (Fig. 1c, Supplementary Figs. 2f-g). To capture the cellular-level effect of the coarse-grained compressive stress obtained from the stress microscopy, we then used Bayesian force inference to compute the relative intracellular pressure and relative interfacial tension at the cellular scale (Figs. 1d-f). This analysis revealed lower interfacial tension (Fig. 1d) and higher intracellular pressure (Figs. 1e-f) in transformed mutant cells as compared to surrounding normal cells at the time when multicellular compressive stress appeared. Together these experiments revealed that while epithelial tissues are generally tensile systems, during the competition between normal and mutant cells, compressive stress arises. This compressive stress precedes the extrusion of transformed mutant cells and is a unique mechanical signature of cell competition.

Distinct characteristics of mutant cells.

To understand why mutant cell colonies experience compressive stress specifically during competition with the wildtype cells, we proposed a physical modeling of a tissue containing a heterogeneous mixture of mutant and wildtype cells using the Self-Propelled Voronoi model (Fig. 1g). However, accurately capturing this heterogeneity requires an understanding of the key differential attributes between the wildtype and mutant populations. These characteristics include homeostatic density, which is the peak density of a confluent monolayer at which the cell division rate becomes negligible, and the integrity of cell-cell junctions.

We first looked at the homeostatic density of these two populations since a differential in homeostatic densities alone can dictate the outcome of two competing populations[24]. To this end, we first quantified homeostatic cell areas within homogeneous confluent monolayers of normal or mutant cells and found that HRas^{V12}-expressing mutant cells exhibit higher homeostatic cell areas than wildtype cells. However, during competition, in the presence of wildtype cells, HRas^{V12}-expressing mutant cells got significantly compacted (Supplementary Fig. 3a). We estimated the competition-associated compaction relative to the homeostatic density by calculating relative compaction as $\Delta\rho = (\rho_c - \rho_h)/\rho_h$ (Supplementary Fig. 3b, Eq. SI-6). We then hypothesized that this compaction could be a consequence of compressive stress and hence, compaction should increase with the increasing compressive stress. To test this hypothesis, we varied the concentration of doxycycline, which led to different levels of

HRas^{V12}-expression. Consequently, the compressive stress also changed, increasing with increasing doxycycline concentration (Supplementary Fig. 3b). Next, plotting the relative compaction with the maximum compressive stress obtained for HRas^{V12}-expressing colonies revealed a nearly linear relationship between the compressive stress and the relative compaction (Supplementary Fig. 3b), indicating a critical consequence of compressive stress on competition-associated compaction of the mutant cells.

We next looked at the integrity of cell-cell junctions in normal and transformed mutant cells. Here we characterized homotypic cell-cell adhesions in wildtype and mutant populations by immunostaining for E-cadherin (Supplementary Figs. 3c-f). We found that in the mutant cells, E-cadherin was localized to cell-cell junctions. In addition, it showed vesicular distribution within the cytoplasm (Supplementary Figs. 3e-f). This cytoplasmic vesicular E-cadherin pool was not observed in the wildtype cells (Supplementary Fig. 3c-d), indicating an instability in cell-cell junctions in the mutant cells. We further corroborated this observation by performing super-resolution spinning-disk confocal microscopy using optical photon reassignment (SoRa)[23] with E-cadherin (stained by an antibody) to show that junctional E-cadherin was significantly deteriorated in the mutant cells as compared to the junctions of wildtype cells (Supplementary Fig. 3g). Alongside, another cell-cell junction protein, alpha-catenin in mutant cells showed a distinct cytoplasmic distribution pattern owing to the reduction in mature adherens junctions. This result reaffirmed the fact that cell-cell junctions were compromised in the mutant cells (Supplementary Figs. 4a-d). Furthermore, live-cell imaging of junctional membranes in a monolayer of mutant cells displayed remarkably dynamic and continuous short-time-scale ruffling whilst junctional membranes in wildtype cells were stable at such short timescales and did not show this peculiar phenotype (Supplementary Figs. 4e-g). These results revealed instability in cell-cell junctions specifically in the mutant cells, while the normal cells showed relatively stable cell-cell adhesions. Surprisingly, we did not observe any significant difference in cell-matrix adhesions, as marked by endogenous paxillin in the two cell types (Supplementary Figs. 4h-j). Taken together, these results elucidated the characteristic differences between the wildtype and mutant cell populations, which we subsequently feed into our computational model.

The computational Self-Propelled Voronoi model explains the origin of compressive stress.

To gain deeper understanding of the emergent mechanics resulting from competition, we used a well-known physical model for confluent tissue, the Self-Propelled Voronoi model (SPV) [24-27], to simulate a heterogeneous monolayer. In this model, the heterogeneities in cell types were represented by differences in the single cell-level mechanical parameters that governed each cell (details of the model are outlined in the SI text). These parameters include the single-cell area and perimeter elastic moduli K_A and K_P, and homeostatic preferred cell area and perimeter A_0 and P_0 respectively. We simulated a co-culture of two types of cells in the SPV, in which a circular island of mutant cells (M) was surrounded by wildtype cells (WT) (Fig. 1g). In this study, we specifically investigated the emergent behavior when these properties differed between mutant and wildtype cells, focusing on the differences in K_A, A_0, and P_0 values. In our simulations we therefore set $K_P = 1$ for all cells and use A_0^{WT} as the unit of length. Therefore, the sum total nondimensionalized mechanical energy function for the cell layer (derived from Eq. SI-1 in SI Section F1) is given by:

$$E = \sum_{i \in WT\ cells} (A_i - 1)^2 + (P_i - P_0^{WT})^2 + \sum_{i \in M\ cells} k\,(A_i - A_0^M)^2 + (P_i - P_0^M)^2 \qquad (1)$$

where we have defined the ratio of cell area elasticities $k = K_A^M / K_A^{WT}$.

Based on our experimental findings that wildtype cells maintained their cell-cell junctions and established a durable, quiescent epithelial layer under ordinary circumstances (Supplementary Fig. 3c-d,g and Supplementary Figs. 4a-b,e-j), we assigned a P_0^{WT} value of 3.65 to these cells, which corresponded generically to a rigid jammed cells[28-30]. Simultaneously, the observation from experiments that HRas^{V12}-expressing cells exhibited less stable cell-cell junctions than wildtype cells (Supplementary Figs. 3e-g and Supplementary Figs. 4c-j) implies that the mutant cells should have a larger value of P_0, corresponding to softer unjammed cells. Furthermore, the larger homeostatic regions observed in mutant cells (Supplementary Fig. 3a) implied a larger value of A_0. Taken together, we propose that the competition of cellular junctional properties between M and WT cells can be encoded by a dimensionless cell shape index ($q_0 = P_0/\sqrt{A_0}$). We first investigated the mechanical properties of the model cell layer by computing the hydrostatic pressure (Π) and interaction normal stress (σ_n) for the mutant and wildtype populations and the mechanical tension (T_{ij}) at cell-cell junctions[31] (Eq. SI-3-5 in SI Section F1). We observed that regardless of the size of the circular island, mutant cells exhibited lower junctional tension than wildtype cells when $q_0^M > q_0^{WT}$ (Fig. 1g and Supplementary Fig. 5a). Meanwhile, mutant cells experienced higher homeostatic pressure than wildtype cells when $A_0^M > A_0^{WT}$ and $P_0^M > P_0^{WT}$ (Fig. 1h). Further, we found that wildtype cells exerted compressive stress on mutant cells ($\sigma_M < \sigma_{WT}$) (Supplementary Fig. 5b), with the stress gradient consistently oriented from high in wildtype cells to low in mutant cells. These phenotypic differences at the individual cell level provide the wildtype cells with a significant advantage in exerting compressive stress on the mutant population.

Consistent with the findings from our experiments (Supplementary Figs. 3a-b), the model was able to accurately capture the density compaction observed in the transformed population within a competitive environment. Specifically, using the same compaction parameter $\Delta\rho$ (Eq. SI-6 in SI Section F2), which exhibited positive values when the mutant cells were under compressive stress or elevated pressure (Fig. 1i), the simulations revealed an interesting finding that the increased compaction observed in the transformed population is primarily influenced by the ratio of the single cell area elasticities $k = K_A^M/K_A^{WT}$ (Fig. 1j). To quantify the effect, we calculated the compressibility, $C = \partial\Delta\rho/\partial\Pi$ (carried out in the linear response regime, see SI Section F2 for details). From the results shown in Fig 1j, we observed that when is $k < 1$, the mutant cells exhibit greater compressibility compared to the wildtype cells, whereas for $k > 1$, the compressibility of the wildtype cells exceeds that of the mutant cells. This provides compelling evidence for the crucial role of the elastic properties of tissue in determining its susceptibility to EDAC, which originates from mechanical imbalances at the microscopic cellular level.

Gel compression microscopy (GCM) to measure collective compressibility.

We then assessed whether the wildtype and mutant populations indeed differed in compressibility, as predicted by our theoretical modeling. To be able to reliably measure collective compressibility, we invented a novel biophysical technique termed as Gel Compression Microscopy (Figs. 2a-b and Supplementary Figs. 6a-b; for details see methods) or GCM. Existing methods to study epithelial tissue mechanics rely either on atomic force microscopy-based indentation[32,33], which only measures individual cell cortical stiffness but fails to sample bulk tissue mechanical properties, or on free-hanging monolayer compression, which requires cell-cell junction fidelity to sustain a suspended monolayer of cells[34,35]. As we have observed previously, HRas^{V12}-expressing cells have weak cell-cell junctions. Hence, we ruled out the free-hanging monolayer setup. Therefore, we were motivated to devise a unique technique where one can live-image a compressing monolayer of cells in real-time (Fig. 2b) and quantitate its compressibility at the multicellular scale (Fig. 2e), while the given monolayer rests on a physiologically relevant substrate (Supplementary Figs. 6a-b). The gel compression

microscopy set-up consists of a cell growth-conducive polyacrylamide hydrogel of defined stiffness interfacing with an acrylic acid-based pH-responsive hydrogel (Supplementary Fig. 6a)[36]. The pH-responsive hydrogel expands at a buffer pH above 6 and contracts at a buffer pH below 4. For better control of the separation between the polyacrylamide gel and the pH-responsive gel and for reproducibility, we utilized soft lithography[53] (Fig. 2a and Supplementary Fig. 6b) to micropattern molds of defined shape and size. Next, to carry out compressibility measurements, we cultured the wildtype or HRas^{V12}-expressing mutant cells to confluency on top of the polyacrylamide gel and subsequently immerse the interfacing pH-responsive gel with normal growth medium (pH ~ 7.4) (Supplementary Fig. 6a). Henceforth, the pH-responsive gel expands at a constant rate exerting a constant multicell-scale compressive stress on the wildtype or HRas^{V12}-expressing monolayer grown over the polyacrylamide gel (Fig. 2d). We computed the relative compressibility of the mutant monolayer relative to that of the wildtype monolayer (Figs. 2c and 2e). In our initial experiments, we used the polyacrylamide gel with Young's modulus of 4 kPa, which is a physiologically relevant tissue stiffness[10]. On 4 kPa gel, the wildtype cell monolayer showed a significant and distinctly lower compressibility modulus relative to gel alone (Fig. 2f and Supplementary videos 2, 3). In contrast, the mutant cell monolayer showed no difference in compressibility as compared to the gel-alone control (Fig. 2f and Supplementary video 4). We then wondered whether mutant cells possess a distinct but relatively much smaller compressibility modulus than a 4 kPa gel. To this end, we performed the compressibility experiments with a softer polyacrylamide gel with Young's modulus of 0.87 kPa (Fig. 2g and Supplementary videos 5, 6, 7). Here, we found that the transformed mutant monolayer showed a compressibility modulus which was comparable to this soft gel but, at least, three-folds higher than the wildtype monolayer (Fig. 2h). Taken together, as had been predicted by our simulations (Fig. 1j), the compressibility measurements with gel compression microscopy suggested that there exists a distinctively higher collective compressibility of the mutant population as compared to their wildtype counterpart and that in line with our predictions, forms the basis of competition driven compressive stress during epithelial defense against cancer.

Different regimes of mechanical phenotypes in cell competition.

Our experiments on active compression revealed that the transformed mutant cells exhibit higher bulk tissue compressibility than their wildtype counterparts (Figs. 2f, h), consistent with our previous linear-response measurements (Fig. 1j). This difference in collective tissue elasticity between the competing populations represents a key mechanical cue driving non-proliferative cell competition in events such as EDAC. To further understand the underlying factors that contribute to this competition, we incorporated active compression into the SPV. This was achieved by allowing the wildtype cells to exert an active self-propelled force on the mutant island (Eq. SI-7,8, see SI Section F3 for a detailed discussion), thereby generating collective elastic response. When an active force was applied, the mutant cells experienced compression. By quantifying the relative change in the total area occupied by the mutant cells, we derived the compressive areal strain using Eq. SI-9. This enabled us to calculate the bulk modulus B (Eq. SI-10), which represents the material's response to isotropic compressions (also done in the linear response regime, see SI Section F3 for a detailed discussion). In essence, the bulk modulus of a material is inversely related to its compressibility. We measured B for a small magnitude of the active force (see SI Section F3) and a wide range of values of k, A_0^M and $\delta q_0 = q_0^M - q_0^{WT}$ with $q_0^{WT} = 3.65$ as reported in the SPV modeling section of this work. Fig. 3a illustrates that the differential bulk modulus ($\Delta B = B_M - B_{WT}$) between wildtype and mutant cells are controlled by both k and δq_0. Notably, ΔB increases linearly with $k\ A_0^M$, where the slope is independent of δq_0 (Fig. 3b). After subtracting by an offset that depends on δq_0,

the data collapsed (Fig. 3b inset, see SI Section F3 for details) to a simpler functional relationship between $\Delta B, k\, A_0^M$ and δq_0, given by:

$$\Delta B - b\, \delta q_0 = f(kA_0^M) \tag{2}$$

These results indicate that competition in *cell area elasticity* plays a central role in driving the differences in bulk modulus between M and WT cells. Conversely, the parameter δq_0, which represents competition in cellular junctional properties, exerts a more subordinate influence.

While the bulk modulus provides insights into a tissue's mechanical response to isotropic compression, the shear modulus is essential for evaluating the tissue's reaction to shear forces. Notably, both solid and fluid materials possess a bulk modulus, whereas the shear modulus is a characteristic exclusive to solids. As a material transitions from a solid state to a flow state, its shear modulus diminishes to zero. Here instead of calculating the shear modulus explicitly for M and WT colonies, we used the mean edge tension (Eq. SI-11) as an approximation for the shear modulus (see SI Section F3 for details). Previous research has demonstrated a linear relation between these two quantities[37].

In Fig. 3c-d, we observe that the differential tension ($\Delta\tau = \tau_M - \tau_{WT}$) decreases as δq_0 increases, this occurs for all values of k, which only sets the rate of decrease. Fig. 3d inset demonstrates that the functional relationship between $\Delta\tau$, δq_0, and k for $A_0^M = 1$ exhibits a universal scaling collapse (see SI Section F3 for details) described by:

$$\Delta\tau = k^d\, f(\delta q_0) \tag{3}$$

These results indicate that the competition in cellular junctional properties (δq_0) plays a central role in driving the differences in shear modulus between M and WT cells. Conversely, competition in cell area elasticity (k) exerts a more secondary influence.

Our simulations show that, in addition to differences in homeostatic cell area (A_0), cells can compete via differences in their area elasticity (k) and junctional properties (δq_0). Taken together, in Fig. 3e we propose a phase diagram that identifies four possible regimes of mechanical competition (see SI Section F3 for details). Given that transformed cells exhibit weaker cellular junctions than their wild-type counterparts, our theoretical model predicts a reduced shear modulus for these cells. Simultaneously, their increased compressibility results in lower cell area elasticity, leading to a diminished bulk modulus compared to WT cells. These findings lead to the conjecture that successful EDAC requires the competing populations to emerge as winners in Region II and losers in Region IV (shaded red in Fig. 3e) of this mechano-phenotypic phase diagram.

Role of destabilized cell-cell junctions in mutant cells.

Finally, we attempted to understand the mechanistic basis for this difference in collective compressibility between the mutant and normal cell populations. At the single-cell level, atomic force microscopy experiments have delineated that HRas^{V12}-expressing mutant cells are stiffer than wildtype cells when in an adherent state, whilst they are softer when in loosely attached or suspended form[32,33,38]. In contrast, we found higher collective compressibility in mutant cells. One possible explanation for these two apparently discrepant observations is the weaker cell-cell adhesions in the mutant cells as compared to the wildtype cells. Indeed, junctional E-cadherin mislocalization leading up to weaker cell-cell adhesions, upon Ras transformation, has been shown before[39]. Therefore, it is possible that weak cell-cell adhesions make a collective of mutant cells more compressible than a collective of wildtype cells. Relevantly, it is known that a matrix metalloproteinase-dependent cleavage of the extracellular domain of the cell-cell adhesion protein E-cadherin drives epithelial extrusion[40]. We, therefore, hypothesized that cell-cell adhesions in the HRas^{V12}-expressing mutants could be compromised due to the cleavage of the extracellular domain of E-cadherin. To test this hypothesis, we used DECMA-1 antibody which binds to the extracellular domain of E-cadherin. Upon mild detergent pretreatment, which permeabilizes cell membrane as well as partially disrupts the interaction between two E-

cadherin molecules from the adjacent cells, DECMA-1 detects both cytoplasmic and membrane-bound E-cadherin, provided their extracellular domains are intact. Without the detergent, DECMA-1 detects only those E-cadherin molecules that are not bound to other E-cadherin molecules and have their extracellular domains intact. We stained both wildtype and mutant cells with this antibody with or without the detergent pretreatment. With detergent pretreatment, we found that E-cadherin remains intact at the junctions of the mutant cells and wildtype cells (Fig. 4a). However, without membrane permeabilization, DECMA-1 showed staining only at the junctions of the mutant cells (Fig. 4b). These results revealed that E-cadherin molecules in mutants remains intact but not bound to E-cadherin molecules of the adjacent cells. To understand the reason behind improper E-cadherin coupling, we then studied the dynamics of E-cadherin in live cells expressing a E-cadherin-GFP construct. We observed an enhanced transport of E-cadherin in mutant cells but not in wildtype cells (Fig. 4c and Supplementary video 8), where E-cadherin molecules showed distinct vesicular fingerprints. Interestingly, this enhanced transport was not due to the endocytic awakening[41] since none of the endocytic compartments, including Rab5 for early endosomes, Rab11 for recycling endosomes, Rab7 for late endosomes and LAMP1 for lysosomes, showed any preferential co-localization with E-cadherin in mutant cells (Supplementary Figs. 7a-e).

In addition, using SoRa super-resolution imaging, we had found that junctional E-cadherin significantly deteriorated in the junctions of mutant cells (Supplementary Fig. 3g). To recover the junctional E-cadherin pool in the mutant cells, we overexpressed E-cadherin-GFP in mutant cells. We assumed that E-cadherin overexpression would lead to the recovery of junctional E-cadherin concentration, and because of increased concentration, it would also lead to enhanced coupling of E-cadherin molecules, effectively "gluing" the mutant cells. Super-resolution imaging with SoRa revealed that junctional E-cadherin pool was indeed recovered within wildtype range upon E-cadherin overexpression (Fig. 4d). Further, when we performed traction force microscopy coupled with stress microscopy in the competition setup with wildtype cells and these E-cadherin-GFP overexpressing cells, there appeared to be no compressive stress at the mutant loci (Fig. 4e) unlike what we had observed before with the mutants alone (Fig. 1c). In fact, just by enriching junctional E-cadherin pool, we could rescue the competition dependent compressive stress which the mutants would experience otherwise, when surrounded by wildtype cells (Fig. 4e). Finally, we performed gel compression microscopy to evaluate the collective compressibility of the E-cadherin-GFP overexpressing $HRas^{V12}$-mutants (Supplementary Fig. 8a and Supplementary video 9). Indeed, collective compressibility of these mutants was now rescued to the range of wildtype population (Fig. 4f) and thus explains the rescue in compressive stress when these mutants encounter wildtype cells in their vicinity.

DISCUSSION

In this work, we combined experimental investigation at the very initial stages of carcinogenesis and *in silico* modeling to define the mechanistic and mechanical basis for epithelial defence against cancer (EDAC). We discovered pre-elimination compressive stress, which is unique to cell competition underlying EDAC and henceforth, may be called competition-induced compressive stress (CICS). We also characterized the putative biophysical properties responsible for CICS to show that higher preferred homoeostatic area and compromised adherens-based cell-cell junctions are distinct properties that the mutant cells acquire upon $HRas^{V12}$-transformation. On the other hand, a growth rate difference between the competing populations, which is classically considered to be the driver of cell competition and oncogenesis, did not appear to be a critical factor for EDAC against $HRas^{V12}$-expressing mutant cells. Further, to reconcile these observations in a single framework, we utilizeda computational Self-Propelled Voronoi model to show that a collective compressibility differential might

explain the emergence of compressive stress during EDAC. While the existing tools to quantitate collective compressibility are either too complex, too customized to be implemented, or rely entirely on the impending cellular strength to suspend freely, we developed an inexpensive, physiologically compatible technique called gel compression microscopy (GCM). GCM includes a compliant substrate for monolayer adhesion, whose stiffness can be modulated, and enables real-time measurements of collective compressibility. Using GCM, we showed that the mutant cell population is indeed more compliant to in-plane compression. GCM measurements thus revealed an oncogenic transformation in the epithelial cells leading to a multicellular length-scale change in its material property. Taken together, we present a mechanical picture of EDAC where the oncogenic transformation of a group of cells in an otherwise normal epithelium modulates their cellular biophysical properties making them more compressible as a collective. Subsequently, during EDAC, a local compressive stress emerges at the mutant loci, which leads to a successful defense against cancer.

In this regard, a recent study parameterized differences in cellular-scale measurements during cell competition between wildtype and mutant cells lacking a tumor suppressor protein, Scribble[42]. They used an agent-based model to show that the homeostatic density of the competing cell types primarily governs mechanical cell competition, while the local tissue organization influences the outcome and kinetics of biochemical competition[42]. However, in the absence of direct measurement of forces, a comprehensive understanding of the causal mechanism driving the mechanical cell competition remained missing. In contrast, we first used stress microscopy techniques to discover CICS. Subsequently, our efforts to understand the mechanistic origin of CICS led to the discovery of differential compressibility via computational modeling and the invention of GCM. Hence, our study went much beyond the previous geometric representation of cell competition and elucidated how individual cell mechanics integrate at the multi-cell scale to bring about oncogenic cell elimination through EDAC. Together, it is tempting to speculate that the transformed cells struggle to achieve their desired, higher cellular area while being resisted by the surrounding normal cells, giving rise to CICS.

In the context of stable epithelial monolayers, the factors that trigger cell competition, including the Ras family of proteins, Myc, Toll, and apicobasal polarity proteins, are also involved in modulating junctional tension[8,43-45]. Consistent with these observations, we demonstrate that junctional fidelity in $HRas^{V12}$-expressing mutant cells is aberrant. The most important epithelial cell-cell adhesion protein, E-cadherin, loses its junctional localization upon oncogenic transformation (Supplementary Fig. 3). The membrane-anchored E-cadherin molecules get actively displaced from the junctions of the mutant cells and trafficked through the cytoplasm and not turned over back to the junctions in time, compromising junctional stability (Fig. 4c, Supplementary Fig. 7 and Supplementary video 8). This instability is corroborated by the diffused cytoplasmic occurrence of another protein associated with cell-cell junctional maturation, alpha-catenin (Supplementary Fig. 4). Remarkably, just by enriching the overall pool of available E-cadherin in the mutants, we observed a significant recovery in their collective compressibility, and the CICS disappeared (Figs. 4e-f).

In the paradigm of EDAC, what still remains to be explored is the cellular phenotypes that fundamentally perturb the bulk mechanical elasticity of epithelial cells as they undergo transformation. How changes in cellular morpho-mechanical landscape rewire EDAC, to push it either towards pro-tumorigenic or anti-tumorigenic fate, is an interesting but enigmatic area of immediate investigation. Furthermore, how cell-autonomous and non-cell-autonomous features arise in normal as well as transformed mutant cells to guide mechanobiological patterns of cell competition, remains poorly understood. Finally, it will be interesting to investigate whether compressive stress also appears during EDAC against mutations in other Ras family proteins and whether the underlying mechanism can be generalized beyond EDAC against $HRas^{V12}$-expressing mutant cells. Nevertheless, using a physiologically model system, our

comprehensive study has unveiled the previously enigmatic physical principle and molecular mechanism that underlie cell competition in epithelial tissue's defense against cancer. This breakthrough not only provides crucial insights into the fundamental dynamics of this process but also opens exciting avenues for the emerging field of mechano-medicine. By understanding how mechanical forces and tissue compressibility play a pivotal role in cell competition, we have set the stage for innovative therapeutic strategies that leverage these principles to target and potentially mitigate the spread of cancerous cells within tissues.

ACKNOWLEDGEMENTS

We thank Yasuyuki Fujita for cell lines and Simran Rawal for microfabrication. This work is funded by DBT/Wellcome Trust India Alliance (grant no. IA/I/17/1/503095 to T.D.). We also acknowledge the intramural funds at Tata Institute of Fundamental Research, Hyderabad from the Department of Atomic Energy, India (under Project Identification No. RTI 4007) and the generous funding by the Human Frontier Science Program (HFSP, grant no. RGP0007/2022). This work was also supported in part by the NIGMS of the National Institutes of Health (NIH) under award number R35GM15049 (D.B.) , the National Science Foundation grant DMR-2046683 (D.B. and S.K.), the Center for Theoretical Biological Physics grant PHY-2019745 (D. B.) and funding from the Alfred P. Sloan Foundation (D.B).

AUTHOR CONTRIBUTIONS

D.B. and T.D. supervised the project. P.G., S.P.P., and P.D. performed the experiments. S.K. and D.B. formulated the theoretical model, performed the computer simulations, and analyzed the simulation results. P.G., S.P.P., and T.D. analyzed the experimental results. H.K.S. contributed to the development of Gel Compression Microscopy. P.G., S.K., S.P.P., D.B., and T.D. wrote the manuscript. All authors edited and approved the manuscript.

COMPETING INTERESTS

The authors declare no competing interests.

REFERENCES:

1 Vishwakarma, M. & Piddini, E. Outcompeting cancer. *Nature Reviews Cancer* **20**, 187-198 (2020). https://doi.org:10.1038/s41568-019-0231-8

2 Moreno, E. Is cell competition relevant to cancer? *Nat Rev Cancer* **8**, 141-147 (2008). https://doi.org:10.1038/nrc2252

3 Hogan, C. *et al.* Characterization of the interface between normal and transformed epithelial cells. *Nat Cell Biol* **11**, 460-467 (2009). https://doi.org:10.1038/ncb1853

4 Kon, S. *et al.* Cell competition with normal epithelial cells promotes apical extrusion of transformed cells through metabolic changes. *Nat Cell Biol* **19**, 530-541 (2017). https://doi.org:10.1038/ncb3509

5 Ellis, S. J. *et al.* Distinct modes of cell competition shape mammalian tissue morphogenesis. *Nature* **569**, 497-502 (2019). https://doi.org:10.1038/s41586-019-1199-y

6 Merino, M. M., Levayer, R. & Moreno, E. Survival of the Fittest: Essential Roles of Cell Competition in Development, Aging, and Cancer. *Trends Cell Biol* **26**, 776-788 (2016). https://doi.org:10.1016/j.tcb.2016.05.009

7 Kajita, M. *et al.* Filamin acts as a key regulator in epithelial defence against transformed cells. *Nat Commun* **5**, 4428 (2014). https://doi.org:10.1038/ncomms5428

8 Levayer, R., Hauert, B. & Moreno, E. Cell mixing induced by myc is required for competitive tissue invasion and destruction. *Nature* **524**, 476-480 (2015). https://doi.org:10.1038/nature14684

9 Matamoro-Vidal, A. & Levayer, R. Multiple Influences of Mechanical Forces on Cell Competition. *Curr Biol* **29**, R762-r774 (2019). https://doi.org:10.1016/j.cub.2019.06.030

10 Pothapragada, S. P., Gupta, P., Mukherjee, S. & Das, T. Matrix mechanics regulates epithelial defence against cancer by tuning dynamic localization of filamin. *Nat Commun* **13**, 218 (2022). https://doi.org:10.1038/s41467-021-27896-z

11 Brás-Pereira, C. & Moreno, E. Mechanical cell competition. *Curr Opin Cell Biol* **51**, 15-21 (2018). https://doi.org:10.1016/j.ceb.2017.10.003

12 Levayer, R., Dupont, C. & Moreno, E. Tissue Crowding Induces Caspase-Dependent Competition for Space. *Curr Biol* **26**, 670-677 (2016). https://doi.org:10.1016/j.cub.2015.12.072

13 Wagstaff, L. *et al.* Mechanical cell competition kills cells via induction of lethal p53 levels. *Nat Commun* **7**, 11373 (2016). https://doi.org:10.1038/ncomms11373

14 Nyga, A. *et al.* Oncogenic RAS instructs morphological transformation of human epithelia via differential tissue mechanics. *Sci Adv* **7**, eabg6467 (2021). https://doi.org:10.1126/sciadv.abg6467

15 Basan, M., Risler, T., Joanny, J. F., Sastre-Garau, X. & Prost, J. Homeostatic competition drives tumor growth and metastasis nucleation. *Hfsp j* **3**, 265-272 (2009). https://doi.org:10.2976/1.3086732

16 Shraiman, B. I. Mechanical feedback as a possible regulator of tissue growth. *Proc Natl Acad Sci U S A* **102**, 3318-3323 (2005). https://doi.org:10.1073/pnas.0404782102

17 Li, S., Balmain, A. & Counter, C. M. A model for RAS mutation patterns in cancers: finding the sweet spot. *Nat Rev Cancer* **18**, 767-777 (2018). https://doi.org:10.1038/s41568-018-0076-6

18 Tan, J. L., Ravid, S. & Spudich, J. A. Control of nonmuscle myosins by phosphorylation. *Annu Rev Biochem* **61**, 721-759 (1992). https://doi.org:10.1146/annurev.bi.61.070192.003445

19 Tambe, D. T. *et al.* Collective cell guidance by cooperative intercellular forces. *Nat Mater* **10**, 469-475 (2011). https://doi.org:10.1038/nmat3025

20 Ishihara, S. & Sugimura, K. Bayesian inference of force dynamics during morphogenesis. *J Theor Biol* **313**, 201-211 (2012). https://doi.org:10.1016/j.jtbi.2012.08.017

21 Serra-Picamal, X. *et al.* Mechanical waves during tissue expansion. *Nature Physics* **8**, 628-634 (2012). https://doi.org:10.1038/nphys2355

22 Das, T. *et al.* A molecular mechanotransduction pathway regulates collective migration of epithelial cells. *Nat Cell Biol* **17**, 276-287 (2015). https://doi.org:10.1038/ncb3115

23 Azuma, T. & Kei, T. Super-resolution spinning-disk confocal microscopy using optical photon reassignment. *Opt Express* **23**, 15003-15011 (2015). https://doi.org:10.1364/oe.23.015003

24 Nagai, T. & Honda, H. A dynamic cell model for the formation of epithelial tissues. *Philosophical Magazine B* **81**, 699-719 (2001). https://doi.org:10.1080/13642810108205772

25 Farhadifar, R., Röper, J. C., Aigouy, B., Eaton, S. & Jülicher, F. The influence of cell mechanics, cell-cell interactions, and proliferation on epithelial packing. *Curr Biol* **17**, 2095-2104 (2007). https://doi.org:10.1016/j.cub.2007.11.049

26 Staple, D. B. *et al.* Mechanics and remodelling of cell packings in epithelia. *Eur Phys J E Soft Matter* **33**, 117-127 (2010). https://doi.org:10.1140/epje/i2010-10677-0

27 Bi, D., Yang, X., Marchetti, M. C. & Manning, M. L. Motility-driven glass and jamming transitions in biological tissues. *Phys Rev X* **6** (2016). https://doi.org:10.1103/PhysRevX.6.021011

28 Mitchel, J. A. *et al.* In primary airway epithelial cells, the unjamming transition is distinct from the epithelial-to-mesenchymal transition. *Nature Communications* **11**, 5053 (2020). https://doi.org:10.1038/s41467-020-18841-7

29 Park, J.-A. *et al.* Unjamming and cell shape in the asthmatic airway epithelium. *Nature Materials* **14**, 1040-1048 (2015). https://doi.org:10.1038/nmat4357

30 Bi, D., Lopez, J. H., Schwarz, J. M. & Manning, M. L. A density-independent rigidity transition in biological tissues. *Nature Physics* **11**, 1074-1079 (2015). https://doi.org:10.1038/nphys3471

31 Yang, X. *et al.* Correlating cell shape and cellular stress in motile confluent tissues. *Proc Natl Acad Sci U S A* **114**, 12663-12668 (2017). https://doi.org:10.1073/pnas.1705921114

32 Gullekson, C., Cojoc, G., Schürmann, M., Guck, J. & Pelling, A. Mechanical mismatch between Ras transformed and untransformed epithelial cells. *Soft Matter* **13**, 8483-8491 (2017). https://doi.org:10.1039/c7sm01396e

33 Matthews, H. K. *et al.* Oncogenic Signaling Alters Cell Shape and Mechanics to Facilitate Cell Division under Confinement. *Dev Cell* **52**, 563-573.e563 (2020). https://doi.org:10.1016/j.devcel.2020.01.004

34 Harris, A. R. *et al.* Characterizing the mechanics of cultured cell monolayers. *Proc Natl Acad Sci U S A* **109**, 16449-16454 (2012). https://doi.org:10.1073/pnas.1213301109

35 Wyatt, T. P. J. *et al.* Actomyosin controls planarity and folding of epithelia in response to compression. *Nat Mater* **19**, 109-117 (2020). https://doi.org:10.1038/s41563-019-0461-x

36 Dong, L., Agarwal, A. K., Beebe, D. J. & Jiang, H. Adaptive liquid microlenses activated by stimuli-responsive hydrogels. *Nature* **442**, 551-554 (2006). https://doi.org:10.1038/nature05024

37 Yan, L. & Bi, D. Multicellular Rosettes Drive Fluid-solid Transition in Epithelial Tissues. *Physical Review X* **9**, 011029 (2019). https://doi.org:10.1103/PhysRevX.9.011029

38 Panciera, T. *et al.* Reprogramming normal cells into tumour precursors requires ECM stiffness and oncogene-mediated changes of cell mechanical properties. *Nat Mater* **19**, 797-806 (2020). https://doi.org:10.1038/s41563-020-0615-x

39 Li, Q. & Mattingly, R. R. Restoration of E-cadherin cell-cell junctions requires both expression of E-cadherin and suppression of ERK MAP kinase activation in Ras-transformed breast epithelial cells. *Neoplasia* **10**, 1444-1458 (2008). https://doi.org:10.1593/neo.08968

40 Grieve, A. G. & Rabouille, C. Extracellular cleavage of E-cadherin promotes epithelial cell extrusion. *J Cell Sci* **127**, 3331-3346 (2014). https://doi.org:10.1242/jcs.147926

41 Malinverno, C. *et al.* Endocytic reawakening of motility in jammed epithelia. *Nat Mater* **16**, 587-596 (2017). https://doi.org:10.1038/nmat4848

42 Gradeci, D. *et al.* Cell-scale biophysical determinants of cell competition in epithelia. *Elife* **10** (2021). https://doi.org:10.7554/eLife.61011

43 Meyer, S. N. *et al.* An ancient defense system eliminates unfit cells from developing tissues during cell competition. *Science* **346**, 1258236 (2014). https://doi.org:10.1126/science.1258236

44 Bosveld, F. *et al.* Modulation of junction tension by tumor suppressors and proto-oncogenes regulates cell-cell contacts. *Development* **143**, 623-634 (2016). https://doi.org:10.1242/dev.127993

45 Clavería, C. & Torres, M. Cell Competition: Mechanisms and Physiological Roles. *Annu Rev Cell Dev Biol* **32**, 411-439 (2016). https://doi.org:10.1146/annurev-cellbio-111315-125142

FIGURE LEGENDS

Fig. 1|Competition induced compression of HRas^{V12}-transformed mutant population. a, Heterogenous competing population constituted by wildtype and HRas^{V12} mutant cells (40:1 number ratio) cultured on a 4 kPa polyacrylamide gel. Induction with doxycycline (dox) shows progressive GFP-HRas^{V12} expression and concomitantly, the mutant cells round up to finally extrude out of the monolayer (mutant colony is marked by blue dotted circle), hpi- hours post induction. **b,** Traction force microscopy generated map of the forces exerted by MDCK cells during competition between mutant and wildtype cells (mutant colony is marked by red dotted circle), analysis done post 2 hours of dox induction. **c,** Stress microscopy generated mean normal stress map depicting compressive stress at the mutant loci (marked by red dotted circle) during competition between wildtype and mutant cells, analysis done post 2 hours of induction with dox. Bayesian force inference generated **d,** interfacial tension map, **e,** relative intracellular pressure map during cell competition between wildtype and mutant cells (mutant colony marked by black dotted circle), inference performed post 2 hours induction with dox. **f,** Normalized relative intracellular pressure characterized with Bayesian force inference, plotted from a pool of 3 independent experiments, analysis performed post 2 hours induction with dox. Data are mean±sd. Statistical significance was calculated using Unpaired t-test with Welch's correction. Scale bar, 50 µm for all experimental panels. **g,** The junctional tension at the edges shared by cells in a circular island of mutant (M) cells (which constitute 12% of the total number of cells in a randomly generated ensemble, with the island's diameter being approximately 40% of the length of the box) is significantly lower than that of their surrounding wild-type (WT) counterparts. This is due to the single-cell parameters of the M cells, which include $K_A^M = 0.7, A_0^M = 0.8, P_0^M = 3.8$, which corresponds to a shape index of $q_0^M = P_0^M/\sqrt{A_0^M} = 4.25$ in contrast to the WT cells with parameters $K_A^{WT} = 1.0, A_0^{WT} = 1.0, P_0^{WT} = 3.65$ $(i.e. q_0^{WT} = 3.65)$. As a result, the M colony exhibits lower edge tension and is less rigid than its surrounding WT cells. **h,** The average pressure in the M island (with the same spatial distribution as shown in **Fig. 1g** and coarse-grained over 50 ensembles of initial configurations) is elevated, with single-cell parameters of $K_A^M = 0.7, A_0^M = 1.5, P_0^M = 3.8$. In contrast, the WT cells have the same single-cell parameters as in **Fig. 1g**. **i,** The relative compaction level, denoted by $\Delta\rho = A_0/\bar{A} - 1$, of the M population is a function of the average pressure (Π) and depends on an array of cell area elasticity ratios, $k = K_A^M/K_A^{WT}$. In the M island, an increase in the value of Π is driven by an increase in A_0^M. **j,** The linear-response compressibility, denoted by $C = \frac{\partial\Delta\rho}{\partial\Pi}$, for M and WT cells as a function of k.

Fig. 2|Gel Compression Microscopy reveals a differential collective compressibility between wildtype and transformed mutants. Conceptual representation depicting the **a,** basis and functionality, and **b,** the data acquisition as done when performing Gel Compression Microscopy (GCM). Micropatterned PDMS mould (shown in blue) with a 150 µm polyacrylamide (PAA) gel (shown in teal) casting donut shaped cavity, is mounted on the glass in a 35mm glass bottom dish. pH-responsive gel (shown in yellow) is casted as a slab in the centre of the donut shaped PAA gel. Cells of interest are cultured on top of the collagen-I coated

PAA gel of defined stiffness. During GCM, the pH-responsive gel expands radially outwards and compresses the cells-PAA gel interface in turn, which is imaged in live (depicted by the imaging region of interest (ROI)) **c,** Representative image panels for 4 kPa PAA gel control, MDCK-wildtype (WT) cell monolayer or MDCK-HRas^{V12} mutant cells cultured on 4 kPa PAA gels for GCM. Pre-compression ROIs are shown to depict PAA gel alone or cells-PAA gel interface (marked by yellow dotted lines) as well as their respective Post-compression ROIs representing the respective interfaces after 90 mins of continuous compression (marked by white dotted lines), Scale bar, 50 µm. **d,** Creep analysis where compressive strain (as fraction to the pre-compression perpendicular shift of the interface) incurred during GCM is plotted as a function of the corresponding time of compression in minutes, Data are mean±sd from three independent experiments. **e,** Analytical representation depicting the methodology and equations used to quantitate compressive strain and relative compressibility (relative to the respective PAA gel alone control). **f,** Relative compressibility measurement based on **e,** shows a distinct and lower value for MDCK-WT population whereas MDCK-MT population shows no distinction compared to the PAA gel case. Data are mean±sem from three-four independent experiments. Statistical significance was calculated using Unpaired t-test with Welch's correction. **g,** Representative image panels for 0.87 kPa PAA gel control, MDCK-WT cell monolayer or MDCK-MT cells cultured on 0.87 kPa PAA gels for GCM. Pre-compression ROIs are shown to depict PAA gel alone or cells-PAA gel interface (marked by yellow dotted lines) as well as their respective Post-compression ROIs representing the respective interfaces after 90 mins of continuous compression (marked by white dotted lines), Scale bar, 50 µm. **h,** Relative compressibility measurement based on **e,** shows a distinct and lower value for MDCK-WT population as also seen in **f**. Importantly, MDCK-MT population shows a distinctly lower value compared to the PAA gel alone case but higher than the MDCK-WT case. Data are mean±sem from three-four independent experiments. Statistical significance was calculated using Unpaired t-test with Welch's correction.

Fig. 3|Theoretical modeling reveals different regimes of mechanical phenotypes in cell competition. In the computational simulations, we assessed both the bulk and shear moduli of the cell colonies. The bulk modulus provided insights into a tissue's mechanical response to isotropic compression, while the shear modulus was essential for evaluating the tissue's reaction to shear forces. These mechanical properties were analysed for a wide range of parameters k, A_0^M and δq_0. Here, k encoded competition in cell area elasticities between the cell types. When $k < 1$, the mutant colony was more compressible than the WT cells that surrounded them. On the other hand, δq_0 encoded the competition in cellular junctional properties; when $\delta q_0 > 0$, the mutant cells had weakened cellular junctions compared to the WT cells. **a,** Behavior of the differential bulk modulus ΔB between WT and M cells in the $k - \delta q_0$ plane for $A_0^M = A_0^{WT} = 1$. The black dotted line corresponds to $\Delta B = 0$. **b,** ΔB plotted as a function of $k\, A_0^M$ for a range of δq_0 values. The inset shows $\Delta B - b\, \delta q_0$ as a function of $k\, A_0^M$ for the same data. Here we used $b = 1.7 \pm 0.2$. **c,** The behavior of the differential colony tension $\Delta\tau$ in the $k - \delta q_0$ plane for $A_0^M = 1$. The white dotted line corresponds to $\Delta\tau = 0$. **d,** $\Delta\tau$ plotted as a function of δq_0 for a range of k values (and $A_0^M = 1$). The inset shows $\Delta\tau/k^d$ as a function of δq_0 exhibiting a scaling collapse. Here we find $d = 0.53 \pm 0.12$. Both the scaling parameters in **Fig. 3b** and **Fig. 3d** are obtained by minimizing error functions which we defined to measure the closeness of the respective data sets. **e,** Based on the analysis of **Fig. 3(a-d)**, we predict a phase diagram which qualitatively distinguishes between mechanical phenotypes that are favored in non-proliferative mechanical cell competition. Specifically, a colony of cells with lower δq_0 and higher $k\, A_0^M$ will have a competitive advantage, as they exhibit lower compressibility and higher rigidity. The predicted phase diagram serves as a useful tool for identifying such mechanical phenotypes.

Fig. 4|Compromised E-cadherin based cell-cell junctions in the HRas^{V12}-transformed mutants underlie competition induced compressive stress as well as rescued collective compressibility. a, Representative image panels to show immunostained MDCK-wildtype (WT) or MDCK-HRas^{V12} mutant (MT) cells for E-cadherin extracellular domain marked by DECMA-1. The immunostaining is performed **a,** WITH detergent (TritonX-100) or **b,** WITHOUT detergent to demonstrate the inherent instability in MT-MT junctions but not WT-WT junctions whereas the extracellular domain being intact in either case. Scale bar, 10 µm. **c,** E-cadherin live dynamics are studied in MDCK-WT or -MT cells mildly overexpressing E-cadherin-GFP. Representative differential interference contrast (DIC) and E-cadherin-GFP image panels are shown. Temporal dynamics for each cell-type is shown as a colour projection map where each time stamp is differentially coloured in the 'yellow hot' colour panel and superimposed. Each time frame refers to 5 second imaging window. Scale bar, 5 µm. **d,** Super-resolution spinning-disk confocal microscopy using optical photon reassignment (SoRa) image panels to show endogenous E-cadherin in MDCK-WT, -MT or -MT overexpressing E-cadherin-GFP. Junctional E-cadherin is shown in insets from the three scenarios to depict E-cadherin loss in mutant cells and rescue in mutant cells overexpressing exogenous E-cadherin-GFP. Scale bar, 10 µm for all image panels and 2 µm for all insets. **e,** Traction force microscopy and stress microscopy panels for cell competition between MDCK-WT cells and MDCK-MT cells overexpressing E-cadherin-GFP. Competition induced compressive stress as seen in **Fig. 1c**, is evidently rescued when E-cadherin is supplied exogenously in the mutant cells. Scale bar, 10 µm. **f,** Relative compressibility measurement based on **Fig. 2e,** shows a distinct and lower value for MDCK-WT population whereas MDCK-MT population shows no distinction compared to the PAA gel control, as also seen in **Fig. 2f**. Importantly, MDCK-MT cells overexpressing E-cadherin-GFP show a distinctly similar value to the MDCK-WT case, showcasing genetic rescue to the mechanical phenotype of compressibility differential. Data are mean±sem from three-four independent experiments. Statistical significance was calculated using Unpaired t-test with Welch's correction.

SUPPLEMENTARY FIGURE LEGENDS

Supplementary Fig. 1|Proliferation differential characterization between wildtype and HRas^{V12}-transformed mutant cells. a, Representative image panels for MDCK-wildtype (WT) or HRas^{V12} mutant (MT) cells, cultured for the indicated time points starting from similar seeding density in order to measure their homeostatic number expansion. Scale bar, 10 µm. **b,** Number expansion characterization for MDCK-WT or -MT cells homogenously cultured until the indicated time points. Data are mean±sem from three independent experiments. Statistical significance was calculated using Unpaired t-test with Welch's correction. **c,** Representative image panels to show EdU^{+} cells (marks proliferating cells, as marked by EdU click-tagged with AlexaFluor-594) for MDCK-WT or -MT cells, cultured for the indicated time points starting from a similar seeding density in order to measure their homeostatic growth rate. Scale bar, 10 µm. **d,** EdU^{+} cell fraction measurement for MDCK-WT or -MT cells homogenously cultured until the indicated time points. Data are mean±sem from three independent experiments. Statistical significance was calculated using Unpaired t-test with Welch's correction.

Supplementary Fig. 2|Experimental setup and mechanical characterization of cell competition between wildtype and HRas^{V12}-transformed mutant population. a, Experimental procedure description to set-up MDCK-wildtype (WT) and HRasV12 mutant (MT) competition on a polyacrylamide (PAA) gel of defined stiffness when seeded in 40:1

(WT:MT) number ratio. **b,** Image panels depicting competition between MDCK-WT and -MT cell populations as described in **a**, where mutant cells are seen to be extruding out of the monolayer of cells (mound of mutant cells in the orthogonal view and in the *bottom* pictograph). Scale bar, 50 µm. **c,** Image panels for MDCK-WT, -MT or competition between the two cell-types depicting immunostained endogenous phosphor-Myosin Light Chain 2 (pMLC2) to mark contractile actomyosin. Sharp pMLC2 enrichment is seen around MDCK-MT cells when surrounded by -WT cells but not in homogenous culture conditions. Scale bar, 10 µm. **d,** Pictographic illustration describing the basis for Monolayer stress microscopy. **e,** Pictographic illustration to describe Bayesian force inference. **f-g,** Monolayer stress microscopy-based stress mapping in a homogenous MDCK-WT (**f**) or MDCK-MT (**g**) depicting predominant tensile stressed in such homogenous conditions for either cell-type. Scale bar, 50 µm. **h,** Time course dependent traction force microscopy and monolayer stress microscopy in a progressively competing MDCK-WT and -MT regime. This comprehensive analysis means to show how traction forces and impending stresses develop as a function of the competition time scale (incurred by the increasing time scale of $HRas^{V12}$ induction with doxycycline). Mutant colony is marked by black dotted circle. hpi- hours post induction with doxycycline. Scale bar, 50 µm.

Supplementary Fig. 3|Distinct mechanobiological characteristics of $HRas^{V12}$-transformed mutant cells. a, Cell spreading area preferred by $HRas^{V12}$ mutant (MT) cells under homeostatic conditions (referred to as ρ_h) or under MDCK-wildtype (WT) and MT competition condition (referred to as ρ_c). Scale bar, 10 µm. **b,** Relative compaction, $\Delta\rho$, defined as $\Delta\rho = (\rho_c - \rho_h)/\rho_h$ is determined for competing $HRas^{V12}$-mutant cells under different times of induction (and thus experiencing different levels of compressive stress (plotted in $\Delta\sigma$). Data is represented as the relative compaction with the maximum compressive stress obtained for mutant colonies revealing a nearly linear relationship between compressive stress and relative compaction. Data are mean±sd from three independent experiments. Statistical significance was calculated using Unpaired t-test with Welch's correction. **c,e,** Representative image panels to show immunostained endogenous E-cadherin in MDCK-WT (**c**) or -MT (**e**) cells cultured in homogenous conditions. Insets are shown (marked by red boxes) to represent one cell in each condition. Scale bar, 10 µm for all image panels and 2 µm for all insets. **d,f,** E-cadherin intensity line plots (marked by yellow line) for a MDCK-WT (**d**) or -MT (**f**) cell. Magenta lines in the **c,e** image panels refer to the intensity plot line. DAPI intensity (marked by cyan line) is plotted for reference to the nucleus. Pink boxes refer to the cytosol in each cell. Intensity values are normalized to the highest value within each dataset. E-cadherin shows distinct junctional accumulation in MDCK-WT cell but diffused cytoplasmic signal in MDCK-MT cell. **g,** Super-resolution spinning-disk confocal microscopy using optical photon reassignment (SoRa) image panels to show endogenous E-cadherin in MDCK-WT or MDCK-MT cells. Junctional E-cadherin is shown in insets from the two cell-types to depict E-cadherin loss in mutant cells. Scale bar, 10 µm for all image panels and 2 µm for all insets.

Supplementary Fig. 4|Cell-cell junction fidelity and cell-matrix adhesion characterization in $HRas^{V12}$-transformed mutant cells. Representative panels to show immunostained endogenous α-catenin in (**a**) MDCK-wildtype (WT) and its respective (**b**) intensity line-plot or (**c**) MDCK-$HRas^{V12}$ mutant (MT) and its respective (**d**) intensity line-plot (Magenta line refers to the intensity plot line). Cells are cultured in homogenous conditions. Insets are shown (marked by red boxes) to represent one cell in each condition. Scale bar, 10 µm for all image panels and 2 µm for all insets. DAPI intensity (marked by cyan line) is plotted for reference to the nucleus. Pink boxes refer to the cytosol in each cell. Intensity values are normalized to the highest value within each dataset. α-catenin shows distinct junctional accumulation in MDCK-WT cell but diffused cytoplasmic signal in MDCK-MT cell. **e,** Live-image time-projected panels of fluorescently labelled plasma membranes for MDCK-WT or -MT cells. Loosely

coupled membranes show long-range undulations and can be captured live which is seen as a broadly localized intensity signal in MDCK-MT cells but a collimated, sharply localized intensity signal in MDCK-WT cells and is plotted as an intensity profile in **f,** intensity values are normalized to the highest value within each dataset. Scale bar, 5 μm. **g,** Cell membrane live dynamics are visualized in MDCK-WT or -MT cells with fluorescently labelled plasma membrane and the temporal dynamics for each cell-type is shown as a colour time projection map where each time stamp is differentially coloured (in the pallet shown) and superimposed. Each time frame refers to a 5 second imaging window. **h-i,** Representative image panels depicting Paxillin based cell-matrix focal adhesions in MDCK-WT (**h**) or -MT (**i**) cells cultured in homeostatic conditions. Paxillin puncta are represented in the basal-plane of the cells while mid-plane is shown as a reference to the cells. Scale bar, 10 μm. **j**, Normalized Paxillin^{+} puncta count is estimated by counting the total number of paxillin puncta in the basal-plane for both MDCK-WT and -MT using Fiji's analyze particle tool and plotted. Data are mean±sem from three independent experiments. Statistical significance was calculated using Unpaired t-test with Welch's correction.

Supplementary Fig. 5|Identifying critical factors using the SPV model. a, The junctional tension (Eq. SI-4) at the edges shared by the mutant (M) cells is significantly higher than that of their surrounding wild-type (WT) counterparts when is $q_0^M \left(= P_0^M / \sqrt{A_0^M} = 3.1 \right) < q_0^{WT} (= 3.65)$. **b,** The system exhibits average normal stress in the M island (with the same spatial distribution as shown in Fig. 1h and coarse-grained over 50 ensembles of initial configurations) is lower, indicating M cells experiencing compressive stress from surrounding WT cells. **c,** Contribution of pressure in the normal stress (corresponding to the first term in the right-hand side of Eq. SI-5). **d,** Contribution of cell-edge tension in the normal stress (corresponding to the second term in the right-hand side of Eq. SI-5).

Supplementary Fig. 6|Gel Compression Microscopy (GCM). a, Illustration to pictographically describe the setup for gel compression microscopy (GCM). Each component from the setup is separately labelled in the pictograph. **b,** Image acquired for a live GCM polyacrylamide (PAA) donut-shaped gel prepared under the micropatterned PDMS mould (referred in **Fig. 2a**). **c,** Creep analysis is plotted where compressive strain (as fraction to the pre-compression perpendicular shift of the interface) incurred during GCM is plotted as a function of the corresponding time of compression in minutes. The total duration for compression is 240 minutes where at about 90 minutes of compression, there is a sharp non-linearity in compression for the MDCK-WT population but not mutant population or PAA gel alone condition. Data are mean±sd from three independent experiments.

Supplementary Fig. 7|Characterization of E-cadherin endocytic trafficking in HRas^{V12} transformed mutant cells. Representative image panels for MDCK-wildtype (WT) or MDCK-HRas^{V12} mutant (MT) cells stained for endogenous E-cadherin and counterstained for **a,** Rab5 for early endosomes, **b,** Rab11 for recycling endosomes, **c,** Rab7 for late endosomes, and **d,** LAMP1 for lysosomes. Insets are shown over respective images (marked by white boxes). Cyan arrowheads show E-cadherin^{+} vesicles whereas white arrowheads show respective endocytic-marker^{+} compartment. In either MDCK-WT or -MT case, E-cadherin did not show any preferential co-localization to any of the endocytic compartments. Scale bar, 5 μm for all image panels and 2 μm for all insets. A pictograph depicting the general E-cadherin endosomal trafficking route in living cells on the *right*.

Supplementary Fig. 8|Gel Compression Microscopy (GCM) based collective compressibility measurements for E-cadherin rescue HRas^{V12} transformed mutant population. a, Representative image panels for 4 kPa PAA gel control, MDCK-wildtype (WT) cell monolayer or MDCK-HRas^{V12} mutant cells or MDCK-HRas^{V12} mutant cells overexpressing E-cadherin-GFP, cultured on 4 kPa PAA gels for GCM. Pre-compression ROIs are shown to depict PAA gel alone or cells-PAA gel interface (marked by yellow dotted lines) as well as their respective Post-compression ROIs representing the respective interfaces after 90 mins of continuous compression (marked by white dotted lines), Scale bar, 50 µm.

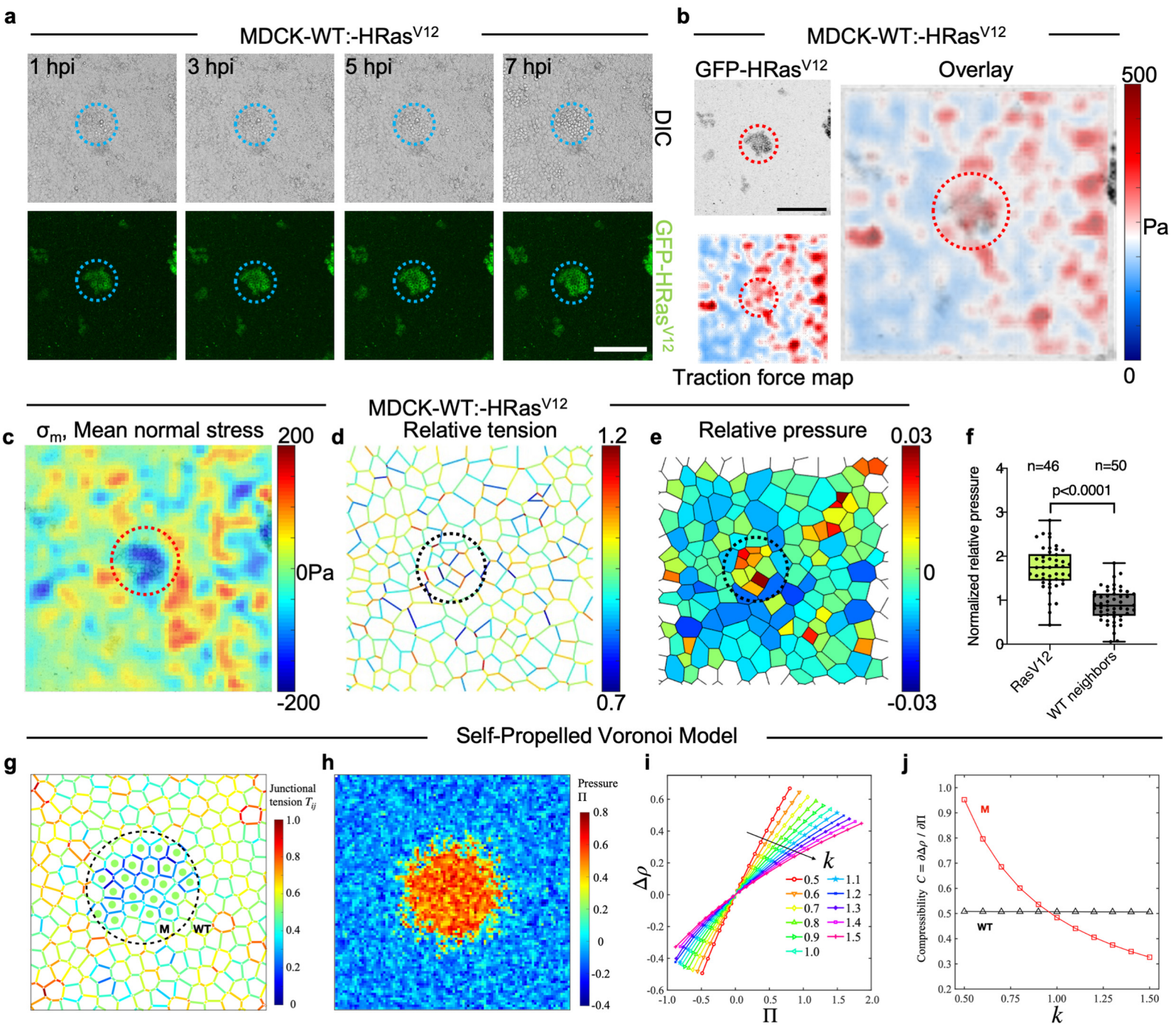
a
MDCK-WT:-HRas^{V12}
1 hpi
3 hpi
5 hpi
7 hpi
DIC
GFP-HRas^{V12}
b
MDCK-WT:-HRas^{V12}
GFP-HRas^{V12}
Overlay
500
Pa
0
Traction force map
MDCK-WT:-HRas^{V12}
c
σ_m, Mean normal stress
200
0Pa
-200
d
Relative tension
1.2
0.7
e
Relative pressure
0.03
0
-0.03
f
n=46
n=50
p<0.0001
Normalized relative pressure
RasV12
WT neighbors
Self-Propelled Voronoi Model
g
Junctional tension T_{ij}
M
WT
h
Pressure Π
i
$\Delta\rho$
Π
k
0.5
0.6
0.7
0.8
0.9
1.0
1.1
1.2
1.3
1.4
1.5
j
Compressibility $C = \partial\Delta\rho / \partial\Pi$
M
WT
k

Figure 1

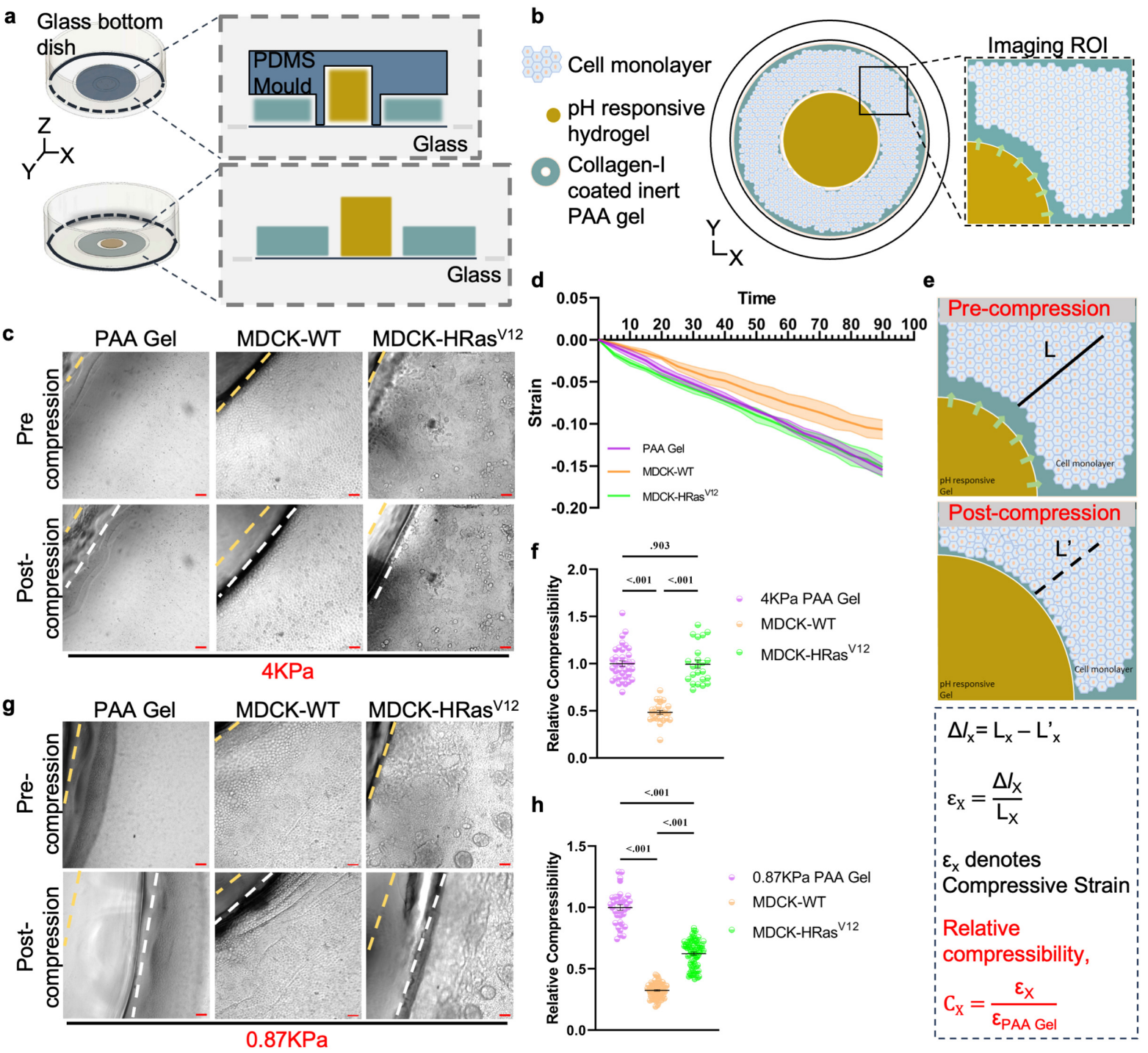
a
Glass bottom dish
PDMS Mould
Glass
Glass
Z
X
Y
b
Cell monolayer
pH responsive hydrogel
Collagen-I coated inert PAA gel
Imaging ROI
Y
X
c
PAA Gel
MDCK-WT
MDCK-HRas^{V12}
Pre compression
Post-compression
4KPa
d
Time
10 20 30 40 50 60 70 80 90 100
0.05
0.00
-0.05
-0.10
-0.15
-0.20
Strain
PAA Gel
MDCK-WT
MDCK-HRas^{V12}
e
Pre-compression
L
Cell monolayer
pH responsive Gel
Post-compression
L'
Cell monolayer
pH responsive Gel
$\Delta l_x = L_x - L'_x$
$\varepsilon_x = \frac{\Delta l_x}{L_x}$
ε_x denotes Compressive Strain
Relative compressibility,
$C_x = \frac{\varepsilon_x}{\varepsilon_{PAA\ Gel}}$
f
.903
<.001
<.001
2.0
1.5
1.0
0.5
0.0
Relative Compressibility
4KPa PAA Gel
MDCK-WT
MDCK-HRas^{V12}
g
PAA Gel
MDCK-WT
MDCK-HRas^{V12}
Pre-compression
Post-compression
0.87KPa
h
<.001
<.001
<.001
1.5
1.0
0.5
0.0
Relative Compressibility
0.87KPa PAA Gel
MDCK-WT
MDCK-HRas^{V12}

Figure 2

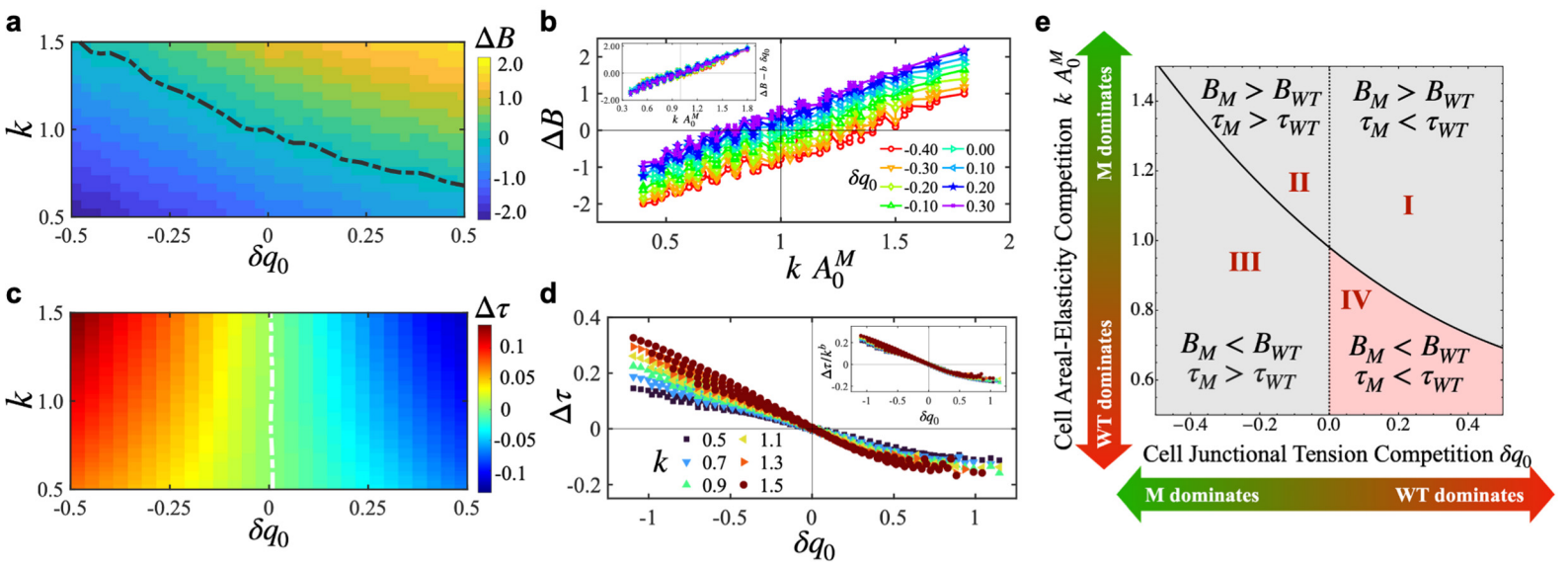
a
b
c
d
e
ΔB
Δτ
k
δq0
k A0M
ΔB − b δq0
Δτ/k^b
-0.40
-0.30
-0.20
-0.10
0.00
0.10
0.20
0.30
0.5
0.7
0.9
1.1
1.3
1.5
Cell Areal-Elasticity Competition k A0M
Cell Junctional Tension Competition δq0
M dominates
WT dominates
I
II
III
IV
B_M > B_WT
τ_M > τ_WT
B_M > B_WT
τ_M < τ_WT
B_M < B_WT
τ_M > τ_WT
B_M < B_WT
τ_M < τ_WT

Figure 3

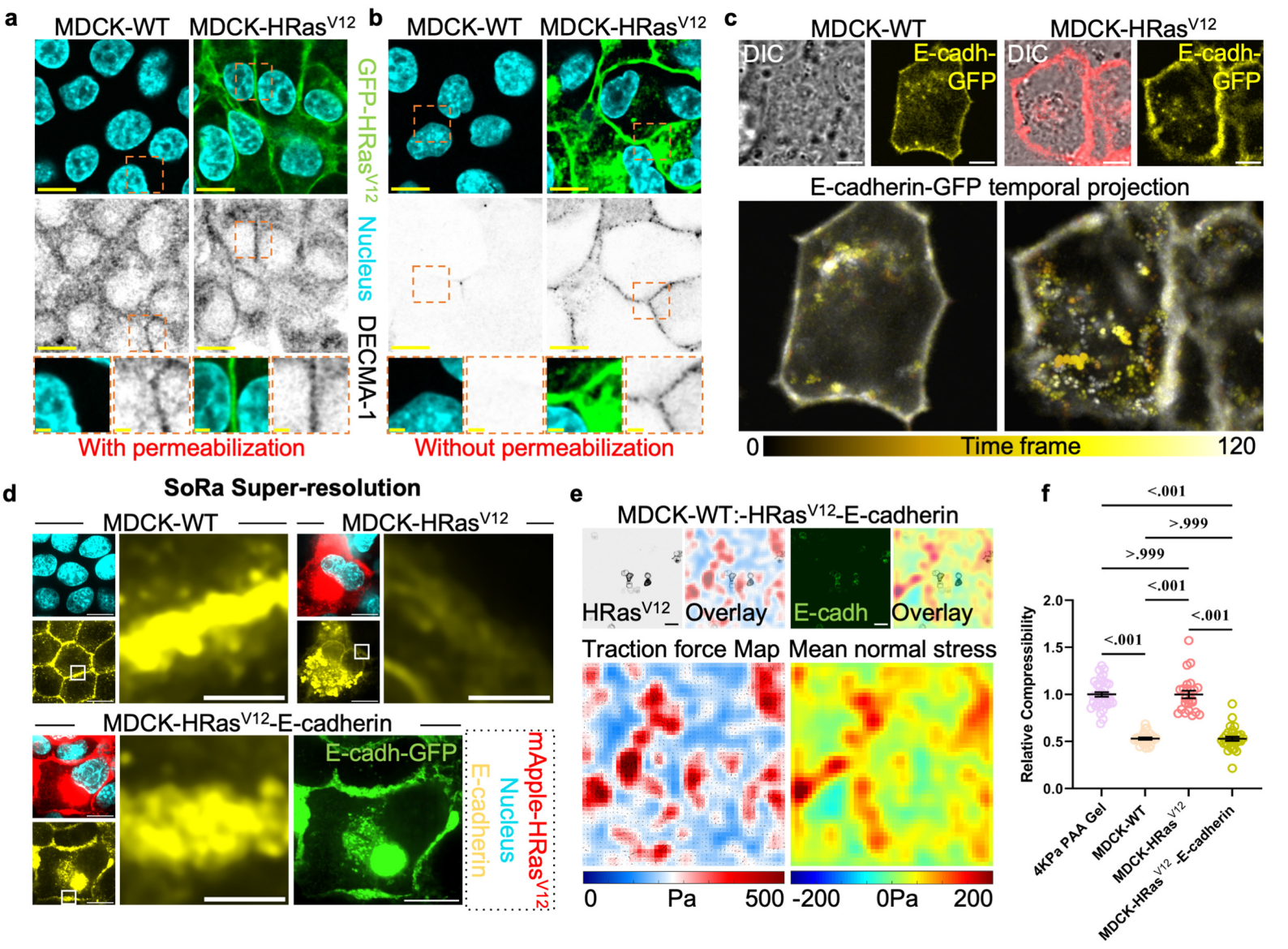
a
MDCK-WT
MDCK-HRasV12
GFP-HRasV12
Nucleus
DECMA-1
With permeabilization
b
MDCK-WT
MDCK-HRasV12
Without permeabilization
c
MDCK-WT
MDCK-HRasV12
DIC
E-cadh-GFP
E-cadherin-GFP temporal projection
0
Time frame
120
d
SoRa Super-resolution
MDCK-WT
MDCK-HRasV12
MDCK-HRasV12-E-cadherin
E-cadh-GFP
mApple-HRasV12
Nucleus
E-cadherin
e
MDCK-WT:-HRasV12-E-cadherin
HRasV12_
Overlay
E-cadh _
Overlay
Traction force Map
Mean normal stress
0
Pa
500
-200
0Pa
200
f
<.001
>.999
>.999
<.001
<.001
<.001
Relative Compressibility
2.0
1.5
1.0
0.5
0.0
4KPa PAA Gel
MDCK-WT
MDCK-HRas V12
MDCK-HRas V12 -E-cadherin

Figure 4